Design, Simulation, And Experimental Validation Of A Varactor-Loaded Reconfigurable Intelligent Surface Unit Cell For Beam Steering At 5.8 Ghz

Roba Walaa El-Din Ahmed and Ashraf S. Abdel-Halim *
Department of Communications and Electronics Engineering, Canadian International College (CIC), Cairo, Egypt
* Corresponding Author: Ashraf_sayed@cic-cairo.edu.eg

Abstract*—Reconfigurable Intelligent Surfaces (RIS) offer a passive, low-power mechanism for shaping the wireless propagation environment, but many reported unit-cell designs stop short of pairing simulated tunability with a fabricated, measured prototype. This paper presents a varactor-loaded RIS unit cell operating at 5.8 GHz, built on a low-cost FR4 substrate and tuned using an SMV1231-079LF hyperabrupt-junction varactor diode placed across a 0.5 mm split gap in an 18 × 18 mm patch. Full-wave simulation in CST Studio Suite, using Floquet-mode analysis under periodic boundary conditions, demonstrates a continuous reflection-phase tuning range of 258° (from −91.7° to +166.3°) as the varactor capacitance is swept from 0 to 1 pF, with stable behavior confirmed under oblique incidence up to 20°. The validated unit cell is then extended to a 4×4 array, in which independently assigned capacitance states generate a spatial phase gradient across the aperture; far-field bistatic scattering simulation confirms beam steering to a main lobe at 161° (approximately 19° from the specular direction), with a 3 dB beamwidth of 26.4° and a side-lobe level of −4.6 dB. A 4×4 hardware prototype was fabricated by conventional PCB manufacturing and characterized using a Rohde & Schwarz ZVB20 Vector Network Analyzer. Measured results show the primary resonance deepening from −8.72 dB (without the RIS) to −11.34 dB (with the RIS positioned in the reflective path), with the resonance frequency shifting from 6.044 GHz to 5.868 GHz, consistently across repeated measurements. Because no active biasing network was implemented for this prototype, hardware validation is limited to S11 characterization rather than a measured phase sweep, and this scope is stated explicitly rather than implied. Together, the results demonstrate a complete, self-consistent design methodology — from unit-cell characterization through array-level beam steering to fabricated hardware validation — for a continuously tunable, low-cost RIS operating in the 5.8 GHz ISM band.

Keywords—Reconfigurable Intelligent Surface; varactor diode; reflection phase; beam steering; metasurface; unit cell array; 5.8 GHz

1. Introduction

The performance of a wireless link is often limited less by the transmitter or receiver than by the channel sitting between them. Multipath reflections, shadowing from walls and other obstacles, and generally unpredictable scattering all chip away at signal quality, and for decades the standard response has been to work around this rather than through it — better antennas, smarter receivers, more transmit power. The channel itself stayed passive. Reconfigurable Intelligent Surfaces (RIS) change that premise. A RIS is a two-dimensional array of subwavelength elements, each capable of altering the phase, amplitude, or polarization of an incident wave, so that the reflected field can be shaped on demand rather than left to chance [1]. That single property is why RIS has attracted so much attention as a low-power, largely passive complement to active relays and phased arrays in 5G, 6G, and IoT systems [1,5].

The earliest working demonstrations used PIN diodes to switch reflection states and proved the basic idea could be built, though usually at the cost of a fairly involved biasing network and non-trivial insertion loss [2]. Since then the field has split roughly into two threads. One is theoretical: papers establishing channel models, phase-shift approximations, and the broader signal-processing framework needed to actually use a RIS in a communication system [5,6]. The other is hardware-driven, and this is where varactor diodes come in — unlike a PIN diode's on/off states, a varactor gives continuous, voltage-tunable capacitance, which translates directly into continuous control over reflection phase [12]. Time-domain coding metasurfaces pushed this further still, showing that a programmable aperture could modulate data directly rather than just redirect a beam [13,14], while holographic and information-metasurface frameworks tried to place all of this within a more general theory of programmable apertures [7,8]. More recent work has turned to what happens once these surfaces are actually deployed — security, multi-user coordination, sensing integration [3,4]. And switching mechanisms other than varactors and PIN diodes have been explored too: light-dependent resistors, for instance, have been used to get bias-free, EMI-resistant phase control built right into an antenna, with beam steering validated experimentally at sub-GHz frequencies [19].

What's missing from a lot of this work, though, is the last mile. Plenty of unit cells are characterized beautifully in simulation and never see a fabricated array [12,13]. Plenty of arrays that do get built rely on discrete switching states rather than the continuous tuning a varactor allows, and even where beam steering is demonstrated at the array level, it isn't always paired with hardware measurements of that same structure [2,19]. So there is a real gap for a design that ties all three pieces together: a quantified, continuous phase-tuning range at one specific frequency of practical interest, a full-wave demonstration that this range actually produces array-level beam steering, and a fabricated, measured prototype to check the simulation against.

That is what this paper sets out to do, using a varactor-loaded RIS unit cell operating at 5.8 GHz — inside the ISM band already used by Wi-Fi and increasingly by IoT and 6G candidate links. The unit cell places an SMV1231-079LF hyperabrupt-junction varactor across a narrow split gap in a square copper patch on FR4, characterized in CST Studio Suite with Floquet-mode analysis under periodic boundary conditions. Sweeping the varactor capacitance from 0 to 1 pF produces a continuous phase swing of 258°, from −91.7° to +166.3°, at the target frequency. Scaling this unit cell into a 4×4 array, with different capacitance values assigned across the elements to build a spatial phase gradient, gives a main scattered lobe at 161° — about 19° off the specular direction — with a 3 dB beamwidth of 26.4° and a side-lobe level of −4.6 dB in far-field simulation. A 4×4 prototype was then fabricated on FR4 by conventional PCB manufacturing, populated with the same SMV1231-079LF varactors, and measured with a Rohde & Schwarz ZVB20 VNA. The measured S11 resonance shifts from 6.044 GHz (antenna alone, −8.72 dB) to 5.868 GHz once the RIS sits in the reflective path (−11.34 dB) — direct evidence that the fabricated surface is doing what the simulation says it should. No biasing network was built for this prototype, so the hardware validation here is limited to S11 characterization rather than a measured phase sweep; we say so explicitly rather than leave it implied, and return to what that limits and does not limit in Section 7.

The rest of the paper follows the natural order of the work. Section 2 covers the unit-cell geometry, substrate choice, and varactor integration. Section 3 lays out the CST simulation setup. Section 4 reports the reflection-phase and resonance behavior across the tuning range, along with a parametric and angular-stability check. Section 5 extends the design to the 4×4 array and its far-field beam-steering results. Section 6 covers fabrication and the measurement setup, and Section 7 the measured results, checked against simulation and benchmarked against related work. Section 8 closes with conclusions and what comes next.

2. Unit Cell Design

2.1. Geometry and Structure

The starting point for this design is a fairly conventional idea: a square metallic patch on top of a dielectric substrate, with a full ground plane underneath, working as a reflective element rather than a radiator. What makes it a RIS unit cell rather than just a patch is the split gap cut into the middle of the patch, sized to take a varactor diode — and it is that diode, not the patch geometry on its own, that gives the cell its reconfigurability.

The unit-cell periodicity is the one dimension in this design that follows directly from theory rather than from simulation. For a periodic reflecting surface excited under Floquet-mode conditions, the periodicity L must stay below half the free-space wavelength to keep higher-order Floquet modes — and the grating lobes that come with them — out of the visible region [20]:

$$L \le \lambda_0 /2 = c/2f_0 \quad (1)$$

At the target frequency of 5.8 GHz, this gives $\lambda_0 \approx 51.72$ mm and $\lambda_0/2 \approx 25.86$ mm. The chosen periodicity of 26 mm sits right at this bound, which is why the structure supports only the fundamental reflected mode across the band of interest without introducing spurious scattering.

The patch and gap dimensions, by contrast, do not follow from a closed-form design equation. Unlike a fed, radiating patch antenna, this element is excited by a normally incident plane wave under periodic boundary conditions, and its resonant behavior is set jointly by the patch geometry, the substrate, and the loaded varactor — a combination that standard cavity-model patch formulas do not capture. The patch width (18 mm), the gap width (0.5 mm), and the substrate thickness (1.5 mm) were instead arrived at through a parametric sweep in CST Studio Suite, iterating the geometry until the structure resonated at 5.8 GHz under the nominal varactor bias condition while leaving enough tuning margin for the varactor's full capacitance range to sweep across the target frequency rather than sit off to one side of it. This process, and its sensitivity to each parameter, is examined further in Section 4.3.

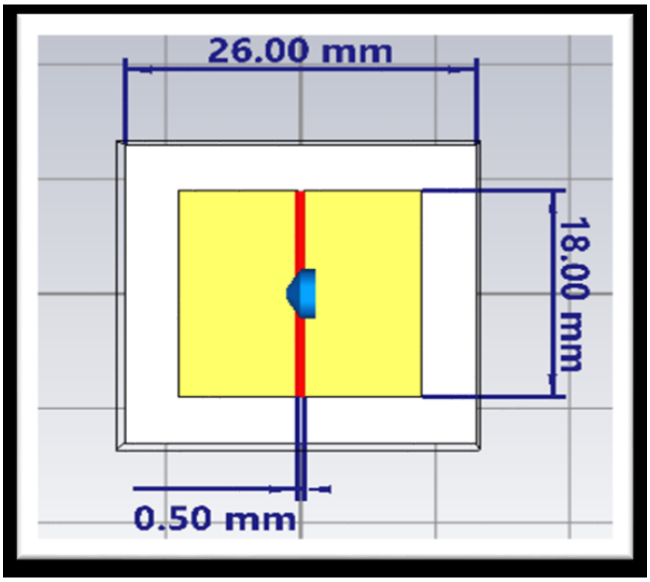

Figure 1. Top-view geometry of the proposed RIS unit cell, showing the 26 × 26 mm periodicity, 18 × 18 mm patch, and 0.5 mm central split gap.

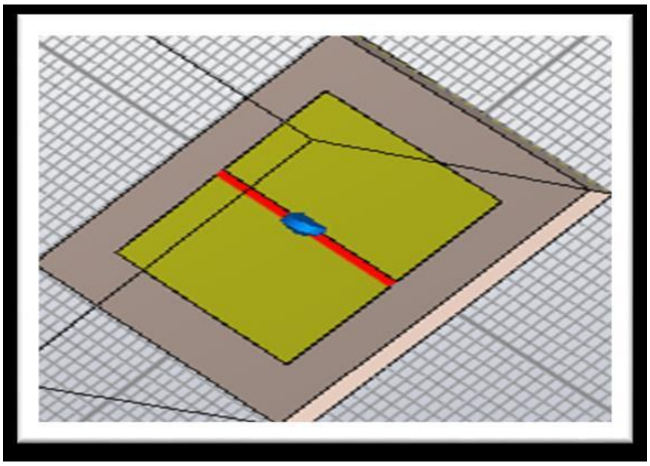

Figure 2. Three-dimensional CST model of the unit cell, showing the copper patch, FR4 substrate, split gap, and ground plane.

Table 1. *Unit cell design parameters.*

Parameter	Description	Value
L	Unit-cell periodicity	26 mm
W	Patch width	18 mm
H	Substrate thickness	1.5 mm
G	Split-gap width	0.5 mm
f_0	Operating frequency	5.8 GHz

2.2. Substrate Selection

FR4 is not the substrate anyone would reach for if minimizing loss were the only goal — Rogers RO4003C or RO4350B would do that job better. It was chosen anyway, for reasons that matter more at the proof-of-concept stage than raw performance does: it is cheap, it is everywhere, and any PCB house can process it without special handling. For a first-generation varactor-loaded RIS meant to validate a design methodology rather than chase record-setting loss figures, that tradeoff made sense.

The relevant electrical property is the relative permittivity, taken as $\varepsilon r \approx 4.3$ for the 1.5 mm-thick substrate used here. That thickness was chosen as a middle ground between impedance behavior, bandwidth, and how forgiving the structure is to fabricate — thinner substrates tighten tolerances in ways that matter once split gaps are being populated with SC-79-package diodes by hand. Copper was used for both the patch and the ground plane, the default choice for conductivity at this frequency. The resonance behavior reported in Section 4 confirms that this substrate and these dimensions do land the structure where intended, close to 5.8 GHz.

2.3. Varactor Integration

The reconfigurability in this design comes entirely from one component: an SMV1231-079LF hyperabrupt-junction varactor diode, placed directly across the 0.5 mm split gap. A varactor is, electrically, a capacitor whose value depends on the reverse bias voltage across it — increase the bias, shrink the depletion region, and the junction capacitance drops. Put one across a gap in a metallic patch, and the patch's resonant behavior becomes something that can be dialed rather than something fixed at design time. That is the entire mechanism this paper relies on.

The varactor was modeled using the manufacturer's lumped-element parameters rather than by simulating the semiconductor junction directly: a series resistance Rv accounting for ohmic loss, a parasitic inductance Lv from the package and bond wire, and the tunable junction capacitance Cv itself. Figure 3 shows where the diode sits — bridging the two halves of the patch across the gap — and Table 2 lists the parameter values used in simulation.

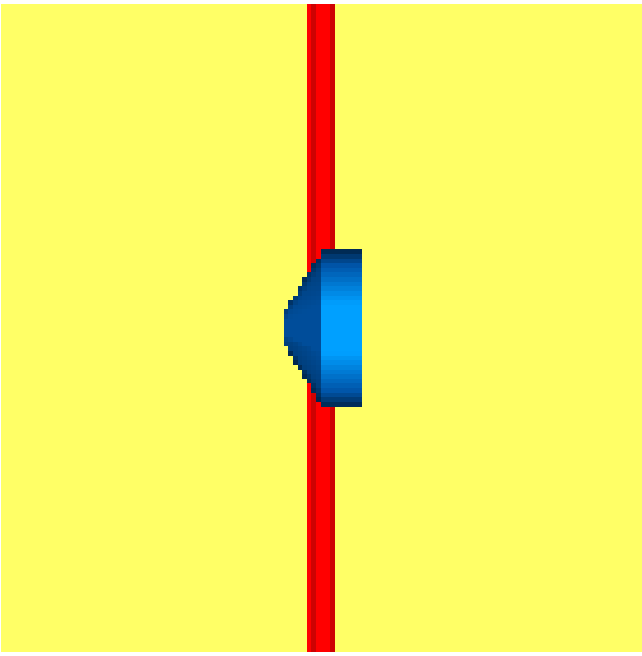

Figure 3. Position of the SMV1231-079LF varactor diode across the split gap, connecting the two halves of the patch.

Table 2. *SMV1231-079LF varactor diode equivalent circuit parameters.*

Parameter	Description	Value
Rv	Series resistance	0.7 Ω
Lv	Parasitic inductance	0.4 nH
Cv	Tunable capacitance range	0–1 pF

2.4. Equivalent Circuit Model

It helps to think of the whole unit cell as a resonant RLC circuit rather than just a patch with a diode placed in it. The patch geometry itself contributes a distributed capacitance and inductance — Cp and Lp — purely from its shape and the way current flows around it. Sitting in parallel with that is the varactor's own series branch: Rv, Lv, and the tunable Cv, all controlled by the bias voltage V. Figure 4 lays this out schematically.

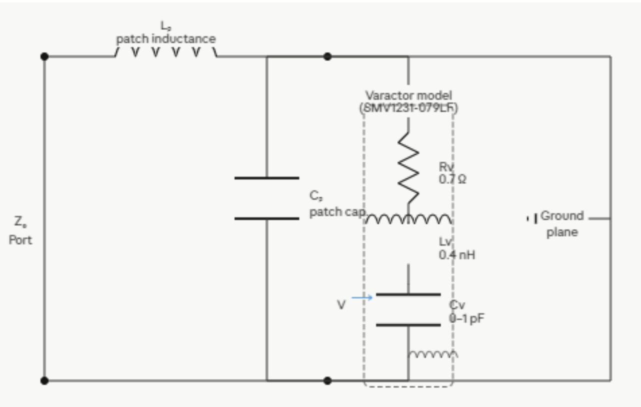

Figure 4. Equivalent RLC circuit model of the unit cell. The left branch represents the distributed patch inductance (Lp) and capacitance (Cp); the right branch (dashed) represents the SMV1231-079LF series model — Rv = 0.7 Ω, Lv = 0.4 nH, Cv = 0–1 pF, set by the bias voltage V.

The reflection behavior of the whole structure is captured by the standard reflection coefficient,

$\Gamma = |\Gamma| e^{(j\varphi)}$ (2)

where |Γ| is the magnitude and φ the phase. What matters for this paper is φ: as Cv moves across its range, the resonant point of the whole RLC network shifts, and φ shifts with it. That is the mechanism behind every result in Section 4.

3. Simulation Methodology

3.1. Solver Setup

All electromagnetic simulation in this work was carried out in CST Studio Suite 2024, using the Frequency Domain Solver. That choice was not automatic — CST offers a Time Domain solver too, and for broadband transient problems it is often the faster option — but for a narrowband resonant structure like this one, where what matters is the S-parameter and phase behavior close to a single target frequency, the Frequency Domain Solver is the more accurate tool for the job, and it is the standard choice for unit-cell characterization in the RIS literature.

The simulation swept 2–7 GHz, wider than strictly necessary if only 5.8 GHz mattered, but the extra range served two purposes. First, it showed how the resonance behaves as the varactor capacitance shifts it around, rather than only capturing whatever happens to fall inside a narrow window. Second, it gave enough margin either side of the target frequency to confirm that 5.8 GHz sits inside a genuine resonance dip rather than on its shoulder. Mesh refinement was handled adaptively — CST iterates the mesh density until the solution converges rather than relying on a single fixed mesh — which matters given how much of the interesting behavior in this structure is concentrated in a very small region: the 0.5 mm split gap and the varactor sitting across it.

3.2. Boundary Conditions and Excitation

The whole point of a unit-cell simulation is to get away with modeling one element instead of an entire array, and that only works if the boundary conditions convince the solver that the single cell is actually sitting inside an infinite periodic surface. This was enforced with Unit Cell (periodic) boundaries on both the x and y faces, which invokes Floquet-mode analysis and lets a single 26 × 26 mm cell stand in for the full aperture. The two z-boundaries do different jobs: the lower one is set to Electric (Et = 0), the correct boundary condition for a solid ground plane, and the upper one is Open (Add Space), which lets the reflected wave propagate away into free space rather than bouncing back into the simulation domain artificially. Table 3 lists the full set.

Table 3. *Boundary conditions applied in the CST Studio Suite unit-cell simulation.*

Boundary	Configuration
Xmin / Xmax	Unit Cell (periodic)
Ymin / Ymax	Unit Cell (periodic)
Zmin	Electric (Et = 0) — ground plane
Zmax	Open (Add Space) — free-space propagation

Excitation was a plane wave, the natural choice given the boundary setup — there is no port or feed line here, just an incident field hitting a reflecting surface. The baseline case uses normal incidence, θ = 0°, φ = 0°, wave travel along the z-axis straight into the structure. That is the configuration behind all of the reflection-phase and resonance results in Section 4. The same sweep was also run at oblique incidence, θ = 20°, specifically to check whether the phase-tuning behavior holds up once the wave is not arriving head-on — real signals do not arrive at a RIS from directly in front of it, so this is not an academic exercise. Those angular-stability results are reported alongside the normal-incidence data in Section 4.4.

4. Reflection Phase and Resonance Results

4.1. Reflection Phase Tunability

The whole premise of this design rests on one question: how much can the reflection phase actually move as the varactor capacitance changes? To answer it, the varactor capacitance Cv was swept across six values — 0, 0.2, 0.4, 0.6, 0.8, and 1.0 pF — and the reflection phase extracted at each point using the Floquet-mode analysis described in Section 3. Figure 5 shows the full phase response across the 2–7 GHz range for all six states, with a vertical marker at 5.8 GHz.

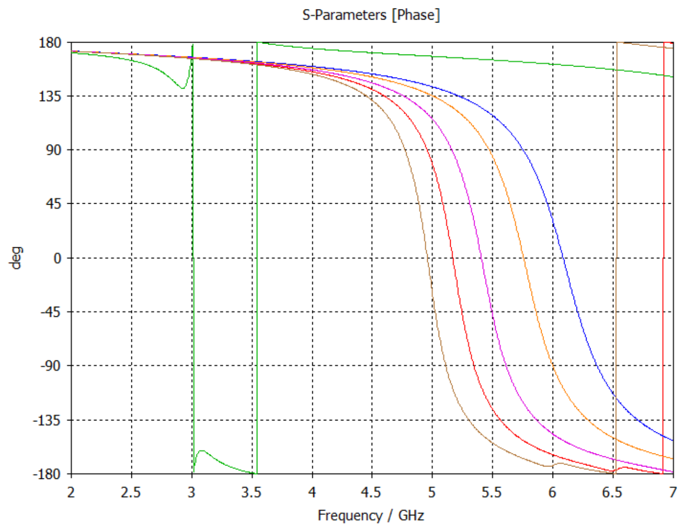

Figure 5. Simulated reflection phase vs. frequency for Cv = 0, 0.2, 0.4, 0.6, 0.8, and 1.0 pF. Each curve shifts toward lower frequency as capacitance increases, reflecting the added reactive loading from the varactor. The vertical line marks the 5.8 GHz target frequency.

Table 4 pulls out the phase value at exactly 5.8 GHz for each capacitance state.

Table 4. *Reflection phase values at 5.8 GHz for different varactor capacitance states.*

Capacitance (pF)	Reflection Phase (°)
0	−10.7
0.2	−91.7
0.4	+166.3
0.6	+55.5
1.0	+17.7

One feature of this table is worth addressing head-on rather than glossing over: the phase does not move monotonically with capacitance. Going from 0.2 pF to 0.4 pF, it jumps from −91.7° to +166.3° — a sharp reversal rather than a smooth continuation. This is not a simulation artifact or an error in the sweep; it is exactly what would be expected from a resonant structure whose resonant frequency is itself sweeping through 5.8 GHz somewhere in that capacitance interval. Near resonance, reflection phase always moves fastest and can appear to wrap across the ±180° boundary — this is standard behavior for varactor-loaded reflective elements and shows up consistently in the literature on tunable metasurfaces [12]. It is a feature of how these structures behave near resonance, not a flaw in this one.

Taking the maximum and minimum phase values across the sweep gives the total achievable tuning range:

$$\Delta\varphi = \varphi max - \varphi min = 166.3° - (-91.7°) = 258° \quad (3)$$

A 258° phase-tuning range at a single fixed frequency is, by itself, the central result of this paper — it is what makes the beam-steering demonstration in Section 5 possible, since generating a usable phase gradient across an array requires individual elements capable of covering a wide swing rather than being locked into two or three discrete states.

4.2. Resonance Analysis

Phase and resonance are two sides of the same coin here, so it is worth looking at the S11 magnitude response alongside the phase data. Figure 6 shows |S11| in dB across the same frequency range and the same six capacitance states.

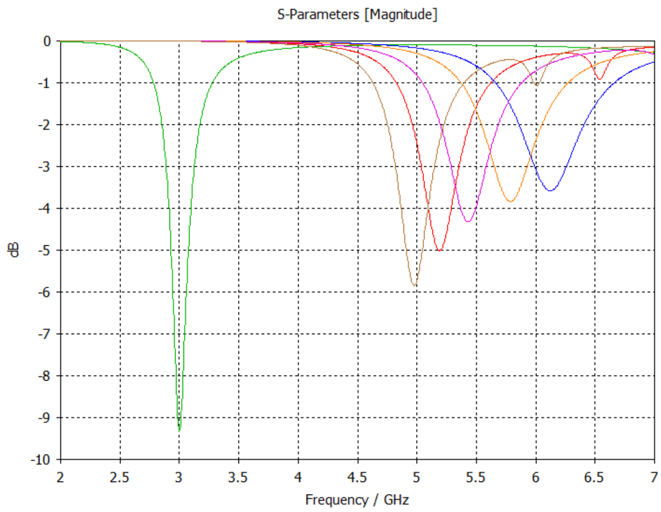

Figure 6. Simulated S11 magnitude (dB) vs. frequency for Cv = 0, 0.2, 0.4, 0.6, 0.8, and 1.0 pF. The resonance dip shifts to lower frequency as capacitance increases.

The pattern here is exactly what the equivalent circuit model from Section 2.4 predicts: increasing Cv adds reactive loading to the resonant network, which pulls the resonance dip toward lower frequencies. This is the same underlying mechanism driving the phase behavior in Section 4.1 — the resonance dip and the rapid phase swing are two measurements of the same physical shift, not independent observations that happen to agree. Deeper resonance dips indicate stronger impedance matching between the incident wave and the structure at that frequency, and the dip depths and positions here are consistent with the substrate and dimensions chosen in Section 2, and with previously reported varactor-loaded metasurface designs more generally [12].

Journal of Multidisciplinary Engineering Science and Technology (JMEST)
ISSN: 2458-9403
Vol. 13 Issue 8, August - 2026

4.3. Parametric Analysis

Three design parameters shape this unit cell's behavior, and it is worth separating out what each one actually controls, since they do not all do the same job.

Capacitance is the parameter that matters most for this paper's purpose, since it is the one under active control — it is what a bias voltage can change in real time, and Section 4.1 already showed just how much reflection-phase range it unlocks (258°, as established above).

Gap width sets how strongly the varactor couples into the patch. A narrower gap concentrates the electric field more tightly across the diode, which generally increases the structure's sensitivity to whatever capacitance the varactor is presenting. The 0.5 mm gap used here reflects a balance between getting strong coupling and staying within what is realistically solderable on an SC-79 package without bridging the gap during assembly, a fabrication concern discussed further in Section 6.

Patch dimensions set where the unloaded resonance sits to begin with. A larger patch pulls resonance down in frequency; a smaller one pushes it up. The 18 × 18 mm patch chosen here places the nominal-bias resonance close enough to 5.8 GHz that the varactor's full 0–1 pF range sweeps across the target frequency rather than sitting entirely above or below it — a restatement, in parametric terms, of the design process already described in Section 2.1.

4.4. Angular Stability

A RIS that only works when a wave arrives exactly perpendicular to its surface is not much use in a real deployment, so the phase sweep was re-run at oblique incidence — θ = 20° — and compared directly against the normal-incidence (θ = 0°) baseline. Figure 7 overlays both sets of curves across all six capacitance states.

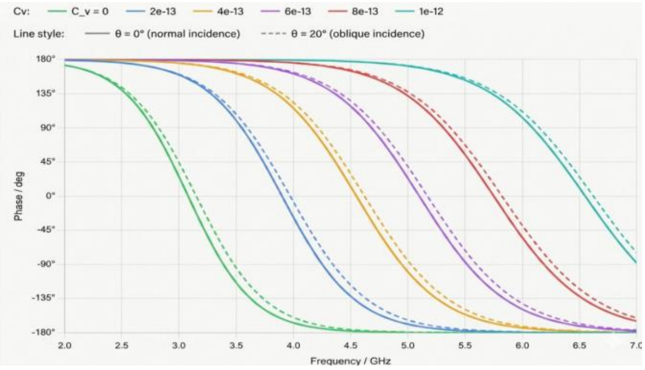

Figure 7. Simulated reflection phase for θ = 0° (solid lines) and θ = 20° (dashed lines) across all capacitance values, Cv = 0 to 1.0 pF. Close agreement between solid and dashed curves at each capacitance confirms angular stability.

The solid and dashed curves track each other closely at every capacitance value, with only minor deviations at θ = 20°. This is the result that was hoped for: it means the phase-tuning behavior this design depends on is not a fragile, boresight-only effect, but holds up reasonably well once the incidence angle moves off-normal — the more realistic condition for a surface meant to redirect signals arriving from somewhere other than straight ahead.

5. Extension to a 4×4 RIS Array

A single unit cell can tell you a lot about phase tunability, but it cannot tell you whether that tunability actually does anything useful once scaled up. Beam steering is fundamentally an array-level phenomenon — it needs a phase gradient across a surface, not just phase range at one point — so this section is where the 258° result from Section 4 either pays off or does not.

5.1. Array Configuration and Geometry

The array was built in CST Studio Suite 2024 by replicating the validated unit cell from Section 2 in a regular 4×4 grid, giving sixteen elements total, each with its own independently biasable varactor. That independence matters: it is what makes it possible to assign a different capacitance state to each column and build a spatial phase gradient across the aperture, rather than having the whole surface move in lockstep.

The array measures 104 mm × 104 mm — four unit cells at the established 26 mm periodicity, in each direction — and otherwise reuses everything from Section 2 unchanged: the same FR4 substrate, the same copper patch geometry, the same ground plane, the same split-gap structure. Nothing about the underlying unit cell was re-optimized for the array. The full-array mesh comprised 159,424 cells, a substantial jump from the unit-cell simulation, reflecting the fact that a periodic-boundary shortcut is no longer available once the solver has to resolve sixteen real, individually excited elements. Figure 8 shows the array as modeled, with all sixteen varactors visible as independent components in the model tree.

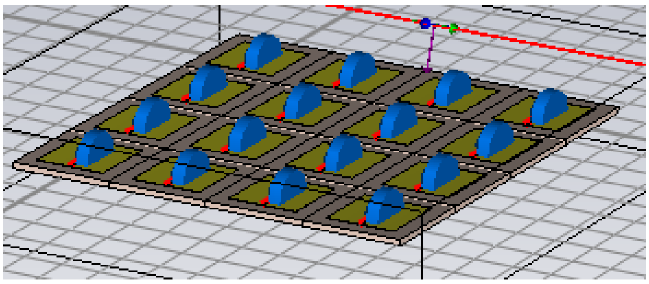

Figure 8. Three-dimensional CST Studio Suite model of the 4×4 varactor-loaded RIS array, showing sixteen independently assigned varactor diodes, one per unit cell.

The incident plane wave was configured at an oblique angle — propagation normal x = 0.342, y = 0, z = −0.94, roughly 20° from the z-axis — deliberately matching the angular-stability configuration already tested at the unit-cell level in Section 4.4. That consistency matters: the beam-steering result

Journal of Multidisciplinary Engineering Science and Technology (JMEST)
ISSN: 2458-9403
Vol. 13 Issue 8, August - 2026

reported below is not generated under some new, untested incidence condition, but under exactly the oblique geometry the unit cell was already shown to handle gracefully.

To build the phase gradient itself, each column of the array was assigned a different capacitance state, shown in Table 5.

Table 5. *Capacitance states assigned across the 4×4 array to generate the spatial phase gradient.*

Column	Capacitance
Column 1	0 pF
Column 2	0.2 pF
Column 3	0.6 pF
Column 4	1.0 pF

These four values are four of the same six states already characterized in Table 4, chosen to span a wide slice of the available 258° phase range across the array's width.

5.2. Surface Current Distribution

Before looking at what the array radiates, it is worth looking at what is actually happening on it. Figure 9 shows the simulated surface current distribution at 5.8 GHz, and the pattern is exactly where the interesting electromagnetic activity would be expected to concentrate: along the edges of each patch, and — more tellingly — right around the split-gap regions where the varactors sit.

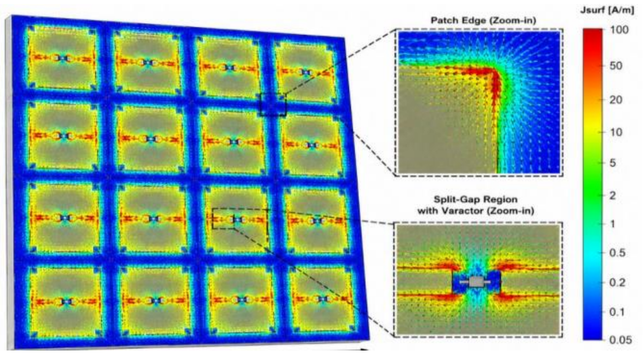

Figure 9. Simulated surface current distribution across the RIS array at 5.8 GHz, with zoomed insets showing current concentration at a patch edge and at a split-gap/varactor region.

That concentration around the gaps is not incidental. It is the current distribution directly confirming that the varactors are doing real electromagnetic work rather than sitting inertly in the structure — each one is visibly influencing the local field pattern around it. Because different columns carry different capacitance values, each column's current pattern differs slightly from its neighbors', which is the current-domain signature of the phase gradient the array is meant to produce.

5.3. Far-Field Beam Steering Results

This is the section where the array either steers a beam or it does not. Figure 10 shows the simulated three-dimensional bistatic radar cross-section (RCS) pattern at 5.8 GHz under plane-wave excitation, and the result is a clearly defined lobe, offset from the specular reflection direction rather than sitting on top of it.

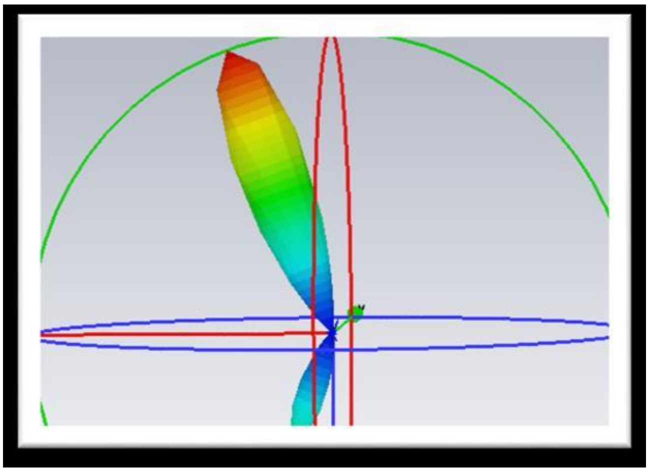

Figure 10. Simulated three-dimensional bistatic RCS pattern of the 4×4 RIS array at 5.8 GHz. The main scattered lobe is visibly displaced from the specular reflection direction, confirming programmable wavefront redirection.

Taking a polar cut through this pattern at $\Phi = 0°$ gives the numbers that characterize the steering: a main lobe at 161°, about 19° away from the specular direction of 180°. That 19° figure aligns closely with the 20° oblique incidence angle configured for the simulation — internal consistency, from a completely different measurement, that the phase gradient across the array is behaving the way the design intends. Table 6 collects the full set of far-field parameters extracted from this simulation.

Table 6. *Far-field performance parameters of the 4×4 RIS array.*

Parameter	Value
Operating frequency	5.8 GHz
Array size	4×4 (16 elements)
Main lobe direction	161° ($\Phi = 0°$ cut)
Steering angle from specular	~19°
3 dB beamwidth	26.4°
Side lobe level	−4.6 dB
Total ACS	0.002442 m^2
Total RCS	0.01793 m^2
Maximum RCS	0.4885 m^2
Simulation type	Bistatic scattering

A 26.4° beamwidth and a −4.6 dB side-lobe level are not record-setting figures on their own, but that is not really the point of this result. What matters is that a 4×4 array — a small, easily fabricated aperture — produces a coherent, well-formed main lobe at all, using nothing but passive capacitance variation across sixteen elements.

5.4. Beam Steering Mechanism

It is worth being explicit about why this works, rather than just reporting that it does. Each unit cell's reflection phase depends on its assigned capacitance, as established in Section 4.1. Assign different capacitances to different columns, and different reflection phases appear at different points across the aperture — a phase gradient, dφ/dx, running across the surface. That gradient deflects the reflected wave according to the generalized form of Snell's law for a phase-gradient surface [6]:

$$\sin(\theta_r) = \sin(\theta_i) + (\lambda/2\pi)(d\varphi/dx) \quad (4)$$

where θ_i and θ_r are the incident and reflected angles, λ is the wavelength, and dφ/dx is the phase gradient across the surface. This is the same relationship underlying anomalous reflection in gradient metasurfaces generally, and it is the reason a 258° tuning range at the unit-cell level was worth demonstrating so carefully in Section 4 — that range is precisely what makes it possible to build a large enough phase gradient across a 4×4 aperture to produce a meaningful, measurable beam deflection. A narrower tuning range would have limited how steep a gradient the array could support, and the steering angle achieved here would very likely have been smaller as a result.

5.5. Scalability: Unit Cell vs. Array Performance

It is worth closing this section by putting the unit-cell and array results side by side, since the whole argument of this paper depends on the claim that one scales cleanly into the other. Table 7 makes that comparison explicit.

Table 7. *Comparison between unit-cell and 4×4 array performance.*

Parameter	Unit Cell	4×4 RIS Array
Operating frequency	5.8 GHz	5.8 GHz
Tuning mechanism	Varactor diode	Varactor diode
Phase tuning range	258°	258°
Number of elements	1	16
Beam steering capability	No	Yes — 19° from specular
Far-field control	Limited	Achieved

The phase-tuning range does not change between the two rows — it cannot, since the array is built from sixteen copies of the same unit cell — but what does change is what that range is for. At the single-element level, a 258° phase swing is just a number describing one component's behavior in isolation. At the array level, that same number becomes the raw material for a phase gradient, and the phase gradient is what actually steers a beam.

6. Fabrication and Hardware Measurement Setup

Simulation can only take a design so far. CST predicts how this structure should behave, but predicting and demonstrating are different things, and the gap between them is exactly what this section exists to close. Everything reported here covers turning the validated 4×4 array design from Section 5 into a physical prototype and setting it up for measurement — the actual measured results, and how they compare against simulation, are covered in Section 7.

6.1. PCB Fabrication and Component Integration

The array was manufactured using standard PCB fabrication on FR4, preserving the exact dimensions established in Section 2 and carried through the array design in Section 5 — nothing was rescaled or adjusted for manufacturability. The finished board carries the copper patch layer on top and the continuous ground plane on the back, with each of the sixteen unit cells retaining its 0.5 mm central split gap, left open and ready to take a varactor. Figure 11 shows the fabricated board before component population.

Figure 11. Fabricated 4×4 RIS PCB array, showing the sixteen copper patch elements on FR4 substrate, each with a 0.5 mm central split-gap region prepared for varactor integration.

Getting from CST model to manufacturable board meant exporting the finalized layout as Gerber files — the standard format PCB houses expect, encoding the copper layers, board outline, and split-gap geometry precisely as simulated. This step is mostly mechanical, but it is worth stating explicitly because it is the point in the workflow where a design stops being a simulation object and becomes a manufacturing instruction; any discrepancy introduced here would propagate silently into the measured results discussed in Section 7.

Journal of Multidisciplinary Engineering Science and Technology (JMEST)
ISSN: 2458-9403
Vol. 13 Issue 8, August - 2026

Once the bare boards came back, the SMV1231-079LF varactors were soldered across each split gap using standard SMD techniques. This is a fussier step than it sounds. The SC-79 package is tiny — roughly 1.0 mm × 0.6 mm — which leaves very little margin for error when placing a component across a gap that is itself only 0.5 mm wide. Solder bridging across the gap was the specific failure mode to avoid, since it would short the two patch halves together and erase the tunable behavior the whole design depends on. Careful, deliberate placement and controlled soldering kept parasitic capacitance and inductance from the joints themselves to a minimum, which matters because those parasitics would otherwise blur the clean resonance behavior established in simulation.

6.2. Experimental Measurement Setup

Electromagnetic characterization of the fabricated array was carried out using a Rohde & Schwarz ZVB20 Vector Network Analyzer, which covers 10 MHz to 20 GHz — comfortably spanning the 5.8 GHz target with plenty of room either side to observe the broader resonance behavior. The VNA was configured over 3–8 GHz for all measurements, with S11 magnitude displayed at 2 dB per division against a −10 dB reference, and up to nine averaging passes applied to suppress measurement noise.

The measurement setup itself consisted of the VNA, an RF calibration kit, coaxial cabling, a mechanical mounting fixture to hold the array steady, and a probe antenna used to illuminate the RIS surface. That probe is worth describing carefully, because it was not a separate, purpose-built antenna brought in from elsewhere: it was the same unit-cell patch geometry described in Section 2, fabricated on identical FR4 substrate, but left without the SMV1231-079LF varactor populated across its split gap. Using the unloaded unit cell as the illuminating probe served a secondary validation purpose alongside its practical one — it confirmed that the same patch geometry underpinning the RIS design is itself electromagnetically functional as a simple resonant radiating element, independent of the tunable loading that gives the full array its reconfigurability. In effect, one design did double duty: as the reconfigurable building block of the array under test, and as the fixed reference antenna used to test it.

Two measurement configurations were used to probe different aspects of the array's behavior. In the first, the probe was placed close against the RIS surface to characterize the direct reflection coefficient at close range. In the second, the probe was moved further back, which allowed observation of how the RIS influences the reflected field once there is real free-space propagation between the two, rather than near-field coupling dominating the measurement. Figure 12 shows both configurations as set up on the bench.

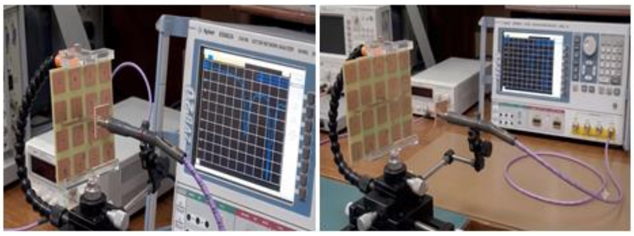

Figure 12. (a) Experimental measurement setup showing the fabricated 4×4 RIS array mounted on a mechanical stand, connected to the Rohde & Schwarz ZVB20 VNA via RF coaxial cable, with the probe positioned at close range to characterize S11. (b) Alternative configuration with the probe positioned at increased distance, used to evaluate the RIS's influence on the reflected field.

6.3. Experimental Validation Procedure

Validation proceeded in two stages, moving from a single element up to the full array — a deliberate mirror of the simulation workflow in Sections 4 and 5, rather than a coincidence of convenience. In the first stage, the VNA was calibrated over the 3–8 GHz range and connected directly to a single fabricated unit cell to check its standalone S11 response before involving the full array. Figure 13 shows the VNA display captured during this initial check, with resonance behavior clearly visible across the 5–7 GHz region.

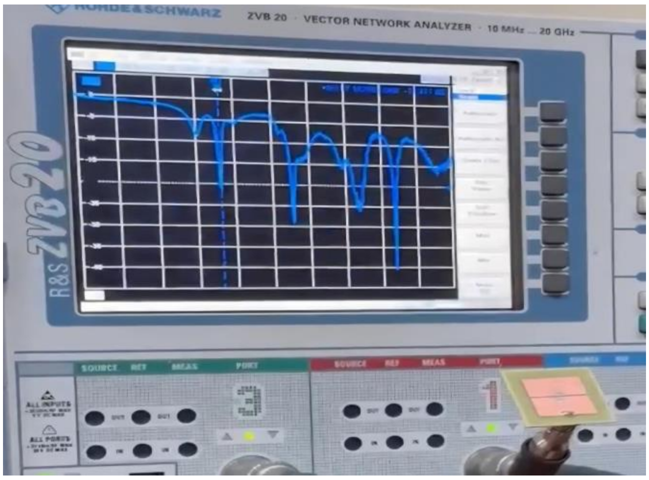

Figure 13. VNA screen capture showing the measured S11 response during initial single-unit-cell characterization, with multiple resonance dips visible across the 3–8 GHz sweep.

The multiple dips visible here are not a concern — they are consistent with the probe interacting with more than one element at different effective coupling distances, exactly the kind of behavior expected once moving from an idealized single-cell simulation to a physical measurement where nearby elements are never perfectly isolated from each other.

In the second stage, the full 4×4 array was measured three separate times, varying the probe-to-surface distance between runs to check that the resonance behavior held up consistently rather than being a one-off artifact of a single measurement setup. Those three S11 traces, and what they show when compared against each other and against the CST predictions from Section 5, are the subject of Section 7.

7. Results and Discussion

7.1. Measured S11 Results

Three sequential S11 measurements were taken with the fabricated 4×4 array, following the two-stage procedure described in Section 6.3. All three used the same VNA configuration — 3–8 GHz sweep, 2 dB/division, −10 dB reference — so the comparison between them is a comparison of the array's behavior, not of three different test conditions.

Measurement 1, taken as the reference case without the RIS contributing to the reflection path, shows a primary dip at 6.044 GHz reading −8.717 dB, with a deeper secondary null at 7.257 GHz reading −19.136 dB. That −8.717 dB primary dip is worth flagging immediately: it does not clear the −10 dB resonance threshold established in Section 4.2, so on its own, this measurement would suggest the structure is not quite resonating strongly enough at this frequency.

Measurements 2 and 3, taken with the RIS positioned in the probe's reflective path, tell a different story. The primary dip deepens to −11.343 dB (at 5.868 GHz) and −11.187 dB (at 6.022 GHz) respectively — both now clearing the −10 dB threshold — and the secondary null at 7.257 GHz deepens too, from −19.136 dB to −23.456 dB and −22.360 dB. Figure 14 shows all three traces for comparison.

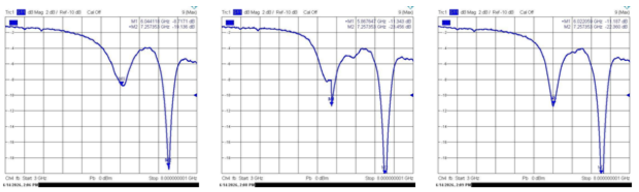

Figure 14. Measured S11 response of the fabricated 4×4 RIS array across three sequential measurements. (a) Reference measurement without RIS contribution: M1 = 6.044 GHz, −8.717 dB. (b) With RIS in the reflective path: M1 = 5.868 GHz, −11.343 dB. (c) Repeat measurement with RIS: M1 = 6.022 GHz, −11.187 dB.

The pattern across all three measurements is consistent rather than coincidental: introducing the RIS into the reflective path makes both resonances measurably deeper, every time. That repeatability matters — a single deep measurement could be noise or a lucky probe placement, but the same effect showing up in Measurements 2 and 3 independently is what turns this from an anecdote into a result.

7.2. Comparison with Simulation

Table 8 lines up the simulated prediction from Section 4 against both the no-RIS and with-RIS measured conditions.

Table 8. *Comparison of simulated and measured S11 parameters.*

Parameter	Simulated (CST)	Measured (No RIS)	Measured (With RIS)
Resonance Frequency	5.8 GHz	~6.0–6.1 GHz	~5.87–6.02 GHz
S11 at Resonance	< −10 dB	−8.7 dB	−11.3 dB / −11.2 dB
Deep Null (secondary)	N/A	−19.1 dB @ 7.26 GHz	−23.5 dB / −22.4 dB @ 7.26 GHz
RIS Effect on S11	N/A	Reference (no RIS)	Enhanced resonance depth confirmed
Frequency Shift vs. Simulation	—	+0.2–0.3 GHz	+0.07–0.22 GHz

Two things are worth separating out here, because they answer different questions. First: does the measured resonance land close to where CST predicted? Broadly yes — within 70–240 MHz, a small fraction of the operating frequency and squarely within the range of deviation expected from FR4's manufacturing-tolerance dielectric constant, PCB etching variation, and the parasitic reactance that soldered SMD joints inevitably add on top of an idealized simulation model. This kind of offset shows up regularly in comparable PCB-based reflective metasurface prototypes reported elsewhere [12,13].

Second, and more central to this paper's argument: does the RIS measurably do something? That is really the question this whole hardware section was built to answer, and the answer is yes — the consistent deepening of S11 once the RIS enters the reflective path is direct, repeatable evidence that the fabricated surface is interacting with and modifying the incident field, exactly as the design intends. It is worth being honest about the limits of that claim, though: because no biasing network was implemented for this prototype, this hardware evidence validates that the RIS reflects and resonates as designed — not that its phase can be actively switched in hardware. The phase-tuning capability itself rests on the simulation results in Section 4; the hardware here confirms the structure's electromagnetic presence and resonance, which is a meaningful but distinct claim.

7.3. Comparison with Related Works

To place this design in context, Table 9 compares it against a PIN-diode-switched metasurface and an LDR-switched RIS-assisted antenna, both drawn from the published literature.

Table 9. *Comparison of the proposed RIS unit cell with previously reported designs.*

Reference	Frequency	Tuning Method	Reconfigurability
PIN-Diode Metasurface [14]	10 GHz	PIN Diode	Discrete Phase States
LDR-Based RIS-Assisted Antenna [19]	0.915 GHz	LDR (optical)	Multi-State Control
Proposed Work	5.8 GHz	Varactor Diode	Continuous — 258° range

The comparison highlights something more useful than simply which design is best, since the three approaches are not really competing for the same job. The PIN-diode approach offers fast, robust switching but only between discrete phase states — typically 1-bit or 2-bit resolution — which caps how fine a phase gradient the surface can produce. The LDR approach trades switching speed for a genuinely elegant simplification: no electrical biasing network at all, since illumination itself drives the reconfiguration, at the cost of also being limited to a handful of discrete states and a comparatively slow response. The varactor-based approach taken in this paper sits in a different part of that trade space entirely: continuous tuning across a measured 258° range, at the cost of needing an active DC bias applied to each element — which is precisely the piece of infrastructure this prototype's hardware validation does not yet include, and the most natural next step for future work.

8. Conclusion and Future Work

8.1. Conclusion

This paper set out to answer a fairly narrow question — can a varactor-loaded RIS unit cell be designed, simulated, scaled into an array, and then actually built and measured, with each stage holding up against the one before it — and the results across Sections 2 through 7 answer that question consistently in the affirmative.

The unit cell itself is unremarkable in isolation: an 18 × 18 mm copper patch on 1.5 mm FR4, with a 0.5 mm split gap carrying an SMV1231-079LF varactor diode, sized at 26 mm periodicity to satisfy the grating-lobe condition for a 5.8 GHz reflective surface. What makes it worth reporting is what happens when the varactor's capacitance is swept: a continuous reflection-phase range of 258°, from −91.7° to +166.3°, extracted from Floquet-mode simulation in CST Studio Suite. That range is not a number that matters on its own — it matters because of what it enables at the next stage.

Extending the same unit cell, unmodified, into a 4×4 array and assigning different capacitance states across its columns produced a genuine steered beam in far-field simulation: a main lobe at 161°, roughly 19° from the specular direction, with a 26.4° beamwidth and a −4.6 dB side-lobe level. The close agreement between that 19° steering angle and the 20° oblique incidence configured for the simulation was the most reassuring single number in this paper — independent confirmation, from a completely different measurement, that the phase-gradient mechanism is behaving the way the underlying theory says it should.

None of that would mean much without hardware to back it up. A 4×4 prototype was fabricated on FR4, populated with SMV1231-079LF varactors across each split gap, and measured with a Rohde & Schwarz ZVB20 VNA. The measured resonance landed within 70–240 MHz of the simulated 5.8 GHz target — a small, explainable offset given ordinary FR4 manufacturing tolerances — and, more importantly, introducing the RIS into the reflective path consistently deepened the measured S11 response across three independent measurements. That repeatable deepening is the closest thing this paper has to direct physical proof that the fabricated surface does what the simulation predicted. It is also worth restating plainly here, rather than leaving it implicit: because no biasing network was built for this prototype, that hardware evidence confirms the RIS's electromagnetic presence and resonance, not a measured phase sweep — the phase-tuning claim rests on the simulation results in Section 4, and the two should not be conflated.

Taken together, the unit-cell design, the array-level beam steering, and the hardware validation form a complete, self-consistent design methodology — one that starts from a single tunable element and ends with a measured board on a bench, with each intermediate step checked against the one before it rather than assumed.

8.2. Major Contributions

The main contributions of this work can be summarized as follows:

1. Design of a compact, varactor-loaded RIS unit cell operating at 5.8 GHz on a low-cost FR4 substrate, with periodicity set by the grating-lobe condition and patch dimensions established through full-wave parametric optimization.

2. Demonstration of a continuous 258° reflection-phase tuning range through varactor capacitance variation, verified across the full 0–1 pF capacitance range with an explicit account of the non-monotonic phase behavior near resonance.

3. Confirmation of angular stability at oblique incidence ($\theta = 20°$), supporting the design's relevance to realistic, non-boresight signal arrival conditions.

4. Extension of the validated unit cell to a 4×4 array without redesign, demonstrating that unit-cell-level phase tunability scales directly into array-level far-field beam steering.

5. Fabrication of a working 4×4 hardware prototype and its experimental characterization via VNA, including a secondary validation in which the

unloaded unit-cell geometry itself served as the illuminating probe antenna.

6. Direct, repeated experimental confirmation that the fabricated RIS measurably alters the reflected field relative to a no-RIS reference condition, with the measured resonance frequency and S11 depth compared quantitatively against simulation.

7. A benchmarking comparison against PIN-diode and LDR-switched RIS designs from the literature, situating the continuous-tuning varactor approach within the broader landscape of RIS reconfiguration mechanisms.

8.3. Future Work

The most immediate limitation of this work — the absence of a biasing network, and with it, a measured hardware phase sweep — is also the most obvious next step. Designing and integrating a DC biasing circuit for each of the sixteen array elements would allow the phase-tuning behavior established here in simulation to be verified directly on the fabricated hardware, closing the one gap between the simulated and measured results reported in Section 7.

Beyond that, several extensions follow naturally from the current design. Larger array configurations — 8×8 or beyond — would improve directivity and steering resolution, at the cost of the additional biasing complexity that comes with more independently controlled elements. It would also be worth comparing the varactor approach taken here directly against PIN-diode, MEMS, or liquid-crystal-based tuning on a matched substrate and frequency, since the comparison in Section 7.3 currently draws on designs built under different conditions rather than a controlled head-to-head test.

Further out, dual-band or broadband RIS architectures would extend this design's usefulness beyond a single operating frequency, and machine-learning-assisted phase optimization could offer a more systematic way of choosing array-wide capacitance states than the column-wise assignment used in Section 5. Given that this design already targets the 5.8 GHz ISM band, integration with emerging 6G systems, intelligent sensing platforms, and broader smart radio environment concepts is a reasonably direct extension rather than a speculative one.

References

1. Q. Wu and R. Zhang, "Towards Smart and Reconfigurable Environment: Intelligent Reflecting Surface Aided Wireless Network," IEEE Communications Magazine, vol. 58, no. 1, pp. 106–112, Jan. 2020.

2. L. Dai, B. Wang, M. Wang, X. Yang, J. Tan, S. Bi, S. Xu, F. Yang, Z. Chen, M. Di Renzo, et al., "Reconfigurable Intelligent Surface-Based Wireless Communications: Antenna Design, Prototyping, and Experimental Results," IEEE Access, vol. 8, pp. 45913–45923, 2020.

3. F. Naeem, M. Ali, G. Kaddoum, C. Huang, and C. Yuen, "Security and Privacy for Reconfigurable Intelligent Surface in 6G: A Review of Prospective Applications and Challenges," IEEE Open Journal of the Communications Society, vol. 4, pp. 1196–1217, 2023.

4. C. Li, K. Weinberger, and A. Sezgin, "A Lightweight Framework for Integrated Sensing and Communications with Reconfigurable Intelligent Surfaces," arXiv:2511.04448, 2025.

5. M. Di Renzo, A. Zappone, M. Debbah, M.-S. Alouini, C. Yuen, J. de Rosny, and S. Tretyakov, "Smart Radio Environments Empowered by Reconfigurable Intelligent Surfaces: How it Works, State of Research, and Road Ahead," IEEE Journal on Selected Areas in Communications, vol. 38, no. 11, pp. 2450–2525, Nov. 2020.

6. E. Björnson, H. Wymeersch, B. Matthiesen, P. Popovski, L. Sanguinetti, and E. de Carvalho, "Reconfigurable Intelligent Surfaces: A Signal Processing Perspective With Wireless Applications," IEEE Signal Processing Magazine, vol. 39, no. 2, pp. 135–158, Mar. 2022.

7. C. Huang, S. Hu, G. C. Alexandropoulos, A. Zappone, C. Yuen, R. Zhang, M. Di Renzo, and M. Debbah, "Holographic MIMO Surfaces for 6G Wireless Networks: Opportunities, Challenges, and Trends," IEEE Wireless Communications, vol. 27, no. 5, pp. 118–125, Oct. 2020.

8. T. J. Cui, S. Liu, and L. Zhang, "Information Metamaterials and Metasurfaces," Journal of Materials Chemistry C, vol. 5, no. 15, pp. 3644–3668, 2017.

9. D. M. Pozar, Microwave Engineering, 4th ed. Hoboken, NJ, USA: Wiley, 2012.

10. C. A. Balanis, Antenna Theory: Analysis and Design, 4th ed. Hoboken, NJ, USA: Wiley, 2016.

11. C. A. Balanis, Advanced Engineering Electromagnetics, 2nd ed. Hoboken, NJ, USA: Wiley, 2012.

12. H.-X. Xu, S. Tang, S. Ma, W. Luo, T. Cai, S. Sun, Q. He, and L. Zhou, "Tunable Microwave Metasurfaces for High-Performance Operations: Dispersion Compensation and Dynamical Switch," Scientific Reports, vol. 6, 38255, 2016.

13. J. Y. Dai, W. K. Tang, J. Zhao, X. Li, Q. Cheng, J. C. Ke, M. Z. Chen, S. Jin, and T. J. Cui, "Wireless Communications through a Simplified Architecture Based on Time-Domain Digital Coding Metasurface," Advanced Materials Technologies, vol. 4, no. 7, 1900044, 2019.

14. L. Zhang, X. Q. Chen, S. Liu, Q. Zhang, J. Zhao, J. Y. Dai, G. D. Bai, X. Wan, Q. Cheng, G. Castaldi, V. Galdi, and T. J. Cui, "Space-Time-Coding

Digital Metasurfaces," Nature Communications, vol. 9, 4334, 2018.

15. A. H. Wheeb, F. Shaik, and S. Karimullah, "Two Purpose-Oriented RIS-Aided Schemes to Enhance and Evaluate the Performance of Wireless Communication," COJ Electronics & Communications, vol. 3, no. 1, pp. 1–13, 2024.

16. Dassault Systèmes, CST Studio Suite 2024 Documentation, CST AG, Germany, 2024.

17. Skyworks Solutions Inc., "SMV1231-079LF Hyperabrupt Junction Tuning Varactor Datasheet," Skyworks Solutions, 2024.

18. D. M. Pozar, "Microstrip Antennas," Proceedings of the IEEE, vol. 80, no. 1, pp. 79–91, Jan. 1992.

19. M. A. Abed and O. N. Uçan, "Reconfigurable Intelligent Surface-Assisted Antenna Design with Enhanced Beam Steering and Performance Benchmarking," Electronics, vol. 14, 4039, 2025.

20. J. Huang and J. A. Encinar, Reflectarray Antennas. Hoboken, NJ, USA: IEEE Press/Wiley, 2008.